_____

_____

This manuscript is a preprint and will be shortly submitted for publication to a scientific journal. As a function of the peer-reviewing process that this manuscript will undergo, its structure and content may change.

If accepted, the final version of this manuscript will be available via the 'Peer-reviewed Publication DOI' link on the right-hand side of this webpage. Please feel free to contact any of the authors; we welcome feedback.

_____

_____

Dynamic rainfall thresholds for landslide early warning in Progo Catchment, Java, Indonesia

Ratna Satyaningsih[1,2], Victor Jetten[1], Janneke Ettema[1], Ardhasena Sopaheluwakan[2], Luigi Lombardo[1], Danang Eko Nuryanto[2]

[1] Faculty of Geo-Information Sciences and Earth Observation, University of Twente, Enschede, The Netherlands

[2] Agency for Meteorology Climatology and Geophysics (BMKG), Jakarta, Indonesia

Abstract

High spatiotemporal resolution satellite data have been available to provide rainfall estimates with global coverage and relatively short latency. On the other hand, a rain gauge measures the actual rain that falls to the surface, but its network density is commonly sparse, particularly those that record at sub-daily records. These datasets are extensively used to define rainfall thresholds for landslides. This study aims to investigate the use of GSMaP-GNRT and CMORPH-CRT data along with automatic rain station data to determine rainfall thresholds for landslides in Progo Catchment, Indonesia, as the basis for landslide early warning in the area. Using the frequentist method, we derived the thresholds based on 213 landslide occurrences for 2012-2021 in the Progo Catchment. Instead of relying on a fixed time window to determine rainfall events triggering landslides, we consider a dynamic window, enabling us to adapt to the rainfall event responsible for landslides by extending or shortening its duration depending on the persistence of the rainfall signal. Results indicate that both GSMaP-GNRT and CMORPH-CRT products fail to capture high-intensity rainfall in Progo Catchment and overestimate light rainfall measured by rain gauge observations.

Nevertheless, when accumulated to define the rainfall threshold, the overall performance of GSMaP-GNRT and automatic rain station data in Progo Catchment is comparable. The rainfall measured at the stations performed slightly better than the estimated rainfall from GSMaP-GNRT, particularly at a probability exceedance level below 15%. In contrast, CMORPH -CRT performed the worst for all exceedance probabilities. The suitable exceedance probability for early warning purposes in Progo Catchment is 10% if it is based on the automatic rain station data. At this exceedance probability level, the threshold can adequately discriminate triggering/non-triggering rainfall conditions and produces the minimum false alarms and missed events.

Keywords:

rainfall thresholds, landslides, early warning, GSMaP-GNRT, CMORPH-CRT

1. Introduction

The complexity of the Indonesian landscape and the unique climatic regime the country is exposed to makes it prone to landslides (Kirschbaum et al., 2015). Monsoons frequently discharge large and prolonged amounts of rainfall which in turn is responsible for widespread landslide events, and their numbers have locally seen a significant increase in the last decade (BNPB, 2021). Specifically, 5822 landslides have been documented in Indonesia from 2010 to 2020, out of which, approximately 79% took place solely within Java (BNPB, 2021). As a result, at least 1044 lives were lost, to which an appalling count of 971 people injured, and 119 missings still need to be added. These numbers attest

to the high-risk locals exposed to landslides (Cepeda et al., 2010; Sartohadi et al., 2010; Hadmoko et al., 2017). These studies also stressed the need for a suitable Early Warning System (EWS) meant to inform the population of the threat they may face and the appropriate behaviour to be taken in imminent situations of hydro-morphological danger.

One EWS is already in place in Indonesia (Hidayat et al., 2019), which the rainfall threshold is valid for the whole Indonesian landscape. A single rainfall threshold might be problematic, as it may not reflect the climatic regime responsible for landslide occurrences in such a diverse territory, nor the terrain characteristics of the same. As a result, the warnings issued for specific areas may be unsuitable, thus leading to false alarms or landslide events that have not been forecasted (Guzzetti et al., 2008; Segoni et al., 2014). This issue is relatively common, with numerous examples of national thresholds failing when their performance is assessed on a local basis (Guzzetti et al., 2020). For this reason, scientific efforts have been made to create a spatially distributed network of rainfall thresholds for specific countries. For instance, Wang et al. (2021) subdivided the Chinese landscape according to six geomorphological regions and assigned a different threshold to each one. Moreover, Peruccacci et al. (2017) defined thresholds over environmental sub-zones in Italy clustered based on topography, lithology, land-use, land cover, climate, and meteorology. An example from another tropical country comes from Malaysia, whose territory is divided into six zones, each of them relying on an independent EWS (Althuwaynee et al., 2015). However, even assigning thresholds to sectors of a given country may not be sufficient to support EWS, and an even higher spatial detail may be required.

For operational EWS, rainfall thresholds are derived for territorial units or alert zones surrounding a reference rain gauge (e.g., Lagomarsino et al., 2013; Segoni et al., 2014). This level of spatial resolution implies that local landslide data may be insufficient to compute thresholds. Thus, the robustness of the rainfall threshold analysis should be considered as a function of the local number of landslides in each sub-zone (Lagomarsino et al., 2013; Segoni et al., 2014; Peruccacci et al., 2017). Aside from the number of landslides, their information is also an important element to evaluate. In fact, assigning a landslide date and time of occurrence is not a trivial task, which is at times undertaken by collecting public reports, leading to positional and temporal errors. The assigning is particularly valid at very large scales, such as national and even global ones, where landslides may be heavily underreported (Kirschbaum and Stanley, 2018). However, defining thresholds over large territories also comes with advantages because one can safely rely on satellite products to describe the spatiotemporal rainfall distribution. For instance, Papua New Guinea used TRMM satellite precipitation estimates (Robbins, 2016). Brunetti et al. (2021) showed that rainfall thresholds estimated from satellite products outperformed those derived from ground observations in India. Even Indonesia tested similar data to support its landslide EWS. Specifically, Hidayat et al. (2019) used the Tropical Rainfall Measuring Mission/TRMM rainfall product (Huffman et al., 2007) with a spatial resolution of 0.25°×0.25°. However, the product failed to capture the spatially heterogeneous rainfall patterns due to its coarse resolution (Chikalamo et al., 2020).

Recent developments are attempting to mitigate this issue with new-generation satellite products such as the Japan Aerospace Exploration Agency's (JAXA) Global Satellite Mapping of Precipitation/GSMaP (Kubota et al., 2020) and the Climate Prediction Center/National Oceanic and Atmospheric Administration's (CPC/NOAA) morphing technique (CMORPH) (Xie et al., 2017) ensuring a higher spatial and temporal resolution. However, this is not the only problem with remotely sensed data. In fact, satellite-based thresholds tend to be much lower than the ones based on local rain gauges, making any comparison between the two difficult (Rossi et al., 2017). Chikalamo et al. (2020) have also observed such a difference within an Indonesian catchment. Irrespective of the data one may choose to use, an important element is shared among all the EWS we have described so far. Each

EWS relies on a fixed time window for the threshold to be derived (e.g., Chikalamo et al., 2020). Among landslide EWSs, there may be differences in the time window length, but the threshold definition itself boils down to a fixed rainfall duration. This element is something we consider requires further consideration. Weather systems are dynamic phenomena and do not always manifest with the same characteristics. Therefore, a fixed event duration may imply that a threshold may miss some important characteristics of the precipitation regime and meteorological variability. We argue instead that a more appropriate solution would be a dynamic time window, capable of adapting to the rainfall event responsible for landslides by extending or shortening its duration depending on the persistence of the rainfall signal. Taking into account the continuous nature of such a signal would allow one to respect prolonged dry periods and extended wet ones, without enforcing a predefined and systematic rule to the threshold analysis. The dynamic time window may account for the different meteorological regimes (Brunetti et al., 2010) or the antecedent rainfall that influence the initial state of soil moisture (Hong et al., 2018).

This study aims to derive and evaluate empirical rainfall thresholds for landslides in Progo Catchment using satellite-based precipitation products (SPPs) and rain gauge observations. To achieve this, we first evaluate the performance of SPPs in detecting rainfall measured by rain gauge observations. Then we define rainfall events responsible for landslides by implementing a dynamic time window. Afterwards, we derive rainfall thresholds using the frequentist method (Brunetti et al., 2010) that allows multiple thresholds depending on the exceedance probability level in such a way that optimum for an early warning, i.e. minimum false alarms and missed events. This study fits into the recent Indonesian effort attested by the work of Hidayat et al. (2019) and revised by Yuniawan et al. (2022) to move away from a unique national EWS and instead move towards a nested system, where specific sectors of the country can rely on their local forecast.

2. Study area and data sets
2.1. Study area

The study area is the Progo Catchment, which is located in central Java, Indonesia, and covers an area of approximately 3100 km^2 (Figure 1). The Progo river, the main river, flows through several mountain ranges, such as Sumbing, Sundoro, Merbabu, Merapi, and Menoreh, which are located in Central Java and Yogyakarta Provinces. Those mountain ranges also form boundaries at the west, north, and east sides of the catchment. Like other regions in Java Island, Progo Catchment is predominated by monsoon climate and experiences the wet northwest monsoon from November to March and the dry southeast monsoon from May to September (Aldrian and Susanto, 2003). During the period of 1991-2000, the average annual rainfall in the catchment is 2358 mm.

The complex landscape of the Progo Catchment makes the area prone to multiple natural hazards. For example, Mount Merapi is one of the most active volcanoes in Indonesia and the flanks of Merapi, which are vulnerable to debris flow, are inhabited by more than 50,000 people (Hapsari et al., 2019). In addition, human settlements are found situated on gentle slopes or very steep slope of Menoreh Mountains, the instability of which are aggravated due to slope-cut and -fill practices to build houses (Hadmoko et al., 2010). Tropical Cyclone Cempaka, which hit the southern coast of Java on November 27, 2017 (BMKG, 2017), caused floods and landslides in the catchment among other affected areas.
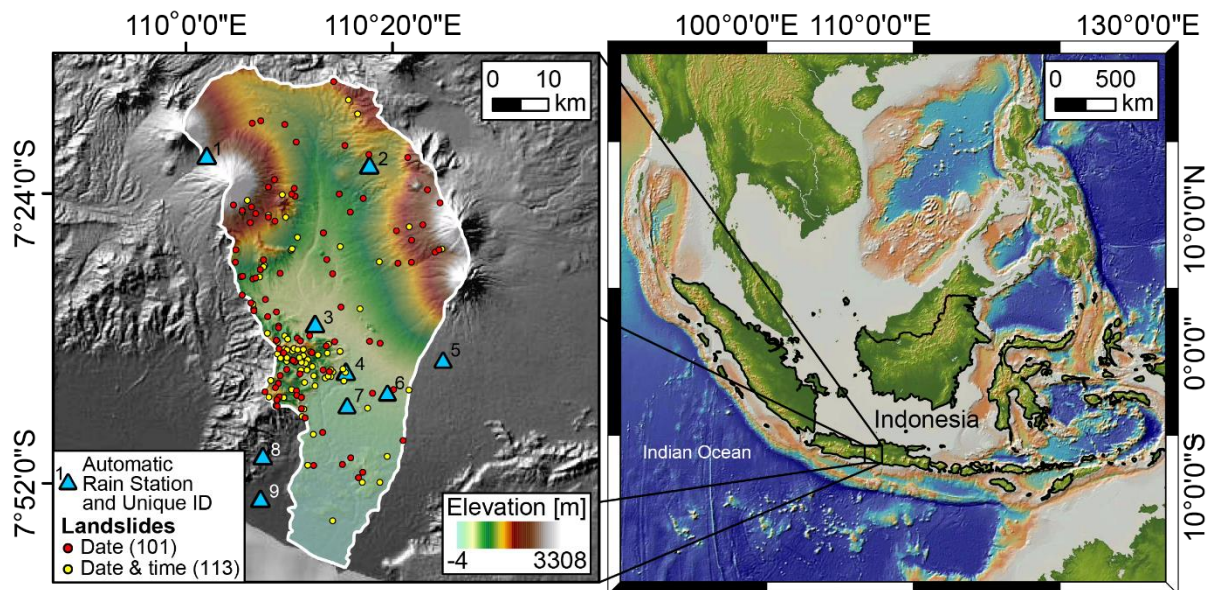
Figure 1. Landslides and automatic rain station locations in the Progo Catchment. The inset shows the location of the Progo Catchment in Java Island, Indonesia. The ID number of automatic rain stations refers to stations presented in Table 1.

2.2. Landslide inventory

We collected landslide information from solely authorised sources, including (i) online reports of landslide events compiled by the National Agency for Disaster Management (BNPB) and Regional Agency for Disaster Management (BPBD), (ii) event reports by the territorial police department, (iii) reports of disaster compiled by the Center for Health Crisis, Indonesian Ministry of Health, and (iv) technical report by the Volcanology Survey Indonesia. We also gathered information on landside occurrences from online mass media. The landslide information collected and stored includes (i) the exact landslide location, (2) the date and the time of the slope failures, (3) the type of landslide, and (4) the trigger. Since most of the reports were prepared by agencies responsible for disaster response, not all information is available in the inventory. The landslide locations are primarily reported by mentioning the name of the governmental administrative unit where the landslide occurred. The administrative unit includes Province, Regency/City, District, Village/Sub-district, and Hamlet, where the province is the highest level, while Hamlet is the lowest one. However, the lowest level of the administrative unit up to which the landslide location reported varied. Only a few reports provided location coordinates. The coordinates are essential for determining objectively the representable rain station for determining rainfall event responsible for a landslide (Section 3.2). Therefore, we geocoded the locations through Google Geocoding API using the ggmap R package (Kahle and Wickham, 2013) based on the names of the administrative units reported. The coordinates are used to select the representative automatic rain gauge station from which the rainfall event triggering the landslide is identified. Since the timing of landslide occurrences is crucial to derive a rainfall threshold, only the landslide events with at least a known date of occurrence are considered.

After reviewing the inventory, we obtained 214 landslide events in the study area from 2012 to 2021, out of which 213 events have a known date of occurrence. Note that multiple events can be triggered for the same rainfall event. For these dated events, the precise or approximate time of landslide occurrence was known for 110 (51.6%) events.

2.3. Rainfall datasets

We used measurements by automatic rainfall stations and rainfall estimates obtained from satellite-based precipitation products (SPPs) to identify the dynamical rainfall thresholds triggering landslides in the study area. The SPPs include the Global Satellite Mapping of Precipitation (GSMaP) data by the Japan Aerospace Exploration Agency (JAXA) and the Climate Prediction Center morphing method (CMORPH) by The National Oceanic and Atmospheric Administration Climate Prediction Center (NOAA CPC). The products are provided by their respective data provider for the World Meteorological Organization (WMO) Space-based Weather and Climate Extremes Monitoring (SWCEM). Kuleshov et al. (2019) demonstrated that the two SPPs provide valuable information for monitoring heavy rainfall over the Maritime Continent.

2.3.1. GSMaP-GNRT data

Global Satellite Mapping of Precipitation (GSMaP) is a blended Microwave-IR product developed by Japan Aerospace Exploration Agency (JAXA) for the Global Precipitation Measurement Mission (GPM). JAXA's GSMaP Near-real-time Gauge-adjusted Rainfall Product version 6 (hereafter GSMaP-GNRT) is processed 4 hours after observation and distributed with a spatial resolution of $0.1° \times 0.1°$ and hourly temporal resolution (Kubota et al., 2020). The dataset is available from April 2000 to the present. For the Southeast Asia region and Pacific Ocean, the data can be obtained from ftp://swcem@hokusai.eorc.jaxa.jp/EAWP/GSMaP_GNRT/DATA/.

While high spatiotemporal resolution data are desirable for landslide study, to our knowledge, the studies that evaluate GSMaP products over the Maritime Continent are typically carried out at a daily scale or even longer timescales up to season (e.g., Kuleshov et al., 2019; Liu et al., 2020; Tashima et al., 2020). Analysis at daily or longer timescales might not reveal the ability of the products to track rapidly evolving extreme rainfall events (Turk and Xian, 2013). Nevertheless, the accuracy of the gauge-adjusted product is generally higher than the uncorrected ones (Kubota et al., 2020; Zhou et al., 2020). A few studies have evaluated the product at a sub-daily scale. Rauniyar et al. (2017) compared several microwave- and infrared-based satellite rainfall data and showed that the gauge-adjusted product outperformed other multi-satellite-based rainfall estimate products in characterising rain-no rain over the Maritime Continent. Moreover, the application in the hydrological modelling also showed that the gauge-adjusted product was more accurate in replicating past flood events in Jakarta, Indonesia, than the uncorrected one (Priyambodoho et al., 2021).

2.3.2. CMORPH-CRT data

The National Oceanic and Atmospheric Administration Climate Prediction Center (NOAA CPC) incorporates precipitation estimates from multiple passive microwave satellites and geostationary satellite infrared data using a technique called CMORPH, Climate Prediction Center morphing method (Joyce et al., 2004). Bias-corrected CMORPH precipitation estimates (hereafter, CMORPH-CRT) are originally generated with a spatial resolution of 8 km × 8 km over the global domain (60°S-60°N) in 30-minute intervals (Xie et al., 2017). For SWCEM, CMORPH-CRT is available from January 1998 to the present with a spatial resolution of $0.1° \times 0.1°$ and temporal resolution of 1-hour. The data are updated at a latency of 2 hours and can be obtained from ftp://ftp.cpc.ncep.noaa.gov/precip/PORT/SEMDP/CMORPH_CRT/DATA/.

The reprocessing and bias-correction of CMORPH original product makes CMORPH-CRT better at representing the magnitude and spatial-temporal variations of precipitation over the quasi-global domain (Xie et al., 2017). This product is similar to the GSMaP-GNRT in the way that both are derived

from PMW observations and adjusted using the CPC gauge-based analysis of global daily precipitation (Chen et al., 2008). The key difference lies in the usage of infrared (IR) dataset. GSMaP derived rainfall estimates from IR data between PMW overpasses (Ushio et al., 2009). Meanwhile, CMORPH retrieves rainfall estimates only from PMW and uses the moving vector of cloud systems derived from IR data to propagate PMW precipitation estimates (Joyce et al., 2004; Xie et al., 2017).

Like GSMaP products, evaluation of CMORPH products was typically performed at a daily scale or longer timescales, including over the Maritime Continent (e.g., Rahmawati and Lubczynski, 2018; Wild et al., 2021). A study at 3-hourly temporal resolution showed that CMORPH-CRT could accurately capture the amplitude of the diurnal cycle over the Maritime Continent (Rauniyar et al., 2017). Using a near real-time CMORPH product, Apip et al. (2010) demonstrated the potential applicability of the product as an input to the hydrological-geotechnical model for a landslide prediction system in the upper Citarum River Catchment, Indonesia.

2.3.3. Automatic rain stations data

The data measured by automatic rain stations were obtained from the Indonesian Agency for Meteorology, Climatology and Geophysics (BMKG). The automatic stations record cumulative rainfall every 10-minute starting from past midnight and ending at midnight Coordinated Universal Time (UTC). The distribution of rain stations with such high temporal resolution in Indonesia is inhomogeneous and sparse in mountainous areas (please see https://awscenter.bmkg.go.id/ for the map of the automatic weather station network). The network density is even sparser than the density of a gauge network that typically measures at 3-hourly and daily periods at the fixed synoptic hours (Kidd et al., 2017).

Before processing the data for analysis, we undertook a test to check gross errors. Missing time intervals were added to create complete 10-minute time series. To detect implausible values, we checked if they fell within a range of 0-300 mm, the measure of the instruments. Values out of range were then manually inspected. If the implausible values were likely caused by mistakes in the algorithm for recording the rainfall value, the values are corrected using the appropriate formula. For instance, in case the values recorded in each 10-minute interval during a day were 10-minute intensity, instead of accumulation, we corrected the value by accumulating from the starting time of accumulation for the day. Otherwise, the values were considered suspicious and excluded from the analysis. If the rainfall is a dip or NA in the time series while the preceding and following values are the same and occur before the accumulate ending hours, the value is set to be the same as the preceding value.

After the gross check, the 10-minute data were aggregated into hourly rainfall to match the lowest temporal resolution of SPPs used in this study. The data were also aggregated into daily data for consistency check with nearby sites. We inspected if the rainfall values > 20 mm/h (very heavy rainfall) had fallen over the site by comparing the daily data to the rainfall of the collocated observations. We accepted the value if the collocated observation exhibited a rainfall event with a comparable amount. Otherwise, we exclude the suspicious value. In the absence of collocated observation, we compared the data with rainfall observations from the neighbouring site(s), which is typically within a distance of ~7 km. In general, comparison with multiple sites was undertaken because of the incompleteness of the data from the nearest site.

Considering the length of rainfall time series and landslide area representativeness, we selected nine automatic rainfall stations located within and nearby the study (Figure 1). The data availability and information of each station are shown in Table 1.

Table 1. Meta-information on the automatic rain stations in the Progo catchment in Central Java, Indonesia

ID	Station name	Lon	Lat	Elevation (meter)	Available period
1	ARG Temanggung	110.0335 °E	7.339445 °S	234	2016-01-01 – present
2	ARG Pakisdadu	110.2957 °E	7.354779 °S	620	2015-08-24 – present
3	ARG SMPK Borobudur	110.2080 °E	7.61007 °S	248	2016-09-01 – present
4	ARG Kalibawang	110.25779 °E	7.687176 °S	160	2017-09-06 – present
5	AWS Pakem	110.4190 °E	7.667140 °S	415	2015-01-01 – present
6	AWS Staklim Mlati	110.3354 °E	7.716165 °S	182	2015-04-01 – present
7	ARG Moyudan	110.2620 °E	7.740457 °S	150	2017-09-06 – present
8	ARG Waduk Sermo	110.123754 °E	7.823245 °S	169	2017-09-06 – present
9	AWS Kulonprogo	110.1202 °E	7.89177 °S	8	2016-11-01 – present

3. Method

The rainfall estimates of SPPs are indirect measurements of rain rates. Hence, we first benchmark the performance of SPPs against the surface measurements in the study area. Considering the availability of the automatic rainfall data, the performance evaluation was carried for period of 1 October 2017-31 December 2021. Afterwards, we identified the rainfall events that triggered past landslides in the study area. Ultimately, we derived the rainfall thresholds based on the cumulated rainfall and the duration of the rainfall events.

3.1. Statistical metrics

We evaluated the detection capacity of SPPs using four indicators based on a common contingency table that includes (i) hit (H), where both SPP and rain station detect the rain occurrence; (ii) miss (M), the rain station detects the rain occurrence, but the SPP does not; (iii) false alarm (FA), SPP detect rain occurrence that does not occur; and (iv) correct negative, neither the rain station nor the SPP detects the rain occurrence. The indicators are the probability of detection (POD), success ratio (SR), bias score (BIAS), and critical success index (CSI). POD indicates the fraction of observed rains that are correctly detected by SPP. SR denotes the fraction of rain occurrences detected by SPP that actually occur. BIAS reflects whether the SPP tends to underestimate (BIAS <1) or overestimate (BIAS >1) rain events. CSI measures the overall fraction of rain occurrences correctly detected by SPP. Those four indicators are summarised in a performance diagram (Roebber, 2009).

To measure the discrepancy between SPP rain estimates and ground observations, we calculated the statistical metrics such as mean absolute error (MAE), relative bias (RB), and correlation coefficient (CC). The formula, range, and perfect score for each metric are listed in *Table 2*. The calculation of the statistical metrics and the visualisation of SPPs performance are carried out using the *verification* R package (NCAR, 2015).

Table 2. Statistical metrics for evaluating the performance of SPPs. Notes: S: SPP rain estimate, O: observed, H: hit, M: miss, FA: false alarm.

Indicator	Formula	Range	Perfect Score
Mean absolute error (MAE)	$MAE = \dfrac{1}{n}\sum_{i=1}^{n}\lvert S_i - O_i \rvert$	$[0,\infty)$	0

Relative bias (RB)	$RB = \dfrac{\sum_i^n (S_i - O_i)}{\sum_i^n O_i}$	$(-\infty, \infty)$	0
Correlation coefficient (CC)	$CC = \dfrac{\sum_i^n (S_i - \bar{S})(O_i - \bar{O})}{\sqrt{\sum_i^n (S_i - \bar{S})^2}\sqrt{\sum_i^n (O_i - \bar{O})^2}}$	$[-1,1]$	1
Probability of detection (POD)	$POD = \dfrac{H}{H + M}$	$[0,1]$	1
Success ratio (SR)	$SR = \dfrac{H}{H + FA}$	$[0,1]$	1
Bias score (BIAS)	$BIAS = \dfrac{H + FA}{H + M}$	$[0,\infty)$	1
Critical success index (CSI)	$CSI = \dfrac{H}{H + M + FA}$	$[0,1]$	1

Following Haile et al. (2013), we calculated the statistical metrics for paired datasets of rainfall rates that are greater than a threshold value of rain detection for at least one of the two datasets. This was carried out to minimise the effects of rainless hours. Rain rates of 0.1 mm/h are considered suitable for defining no-rain conditions since such a low intensity is unlikely to generate surface ponding and runoff (Dunkerley, 2015). To assess the performance of the SPPs in capturing higher rainfall intensities, we extended the rain detection threshold for other values: 0.2 mm/h, 0.5 mm/h, 1 mm/h, 5 mm/h, and 10 mm/h.

3.2. Determination of rainfall events

When the exact or estimated location and the date of landslide events were known, we selected the representable rain station based on the nearest distance. We also considered the station elevation by finding the minimum difference in elevation between the station and the landslide location. However, we prioritised the distance over elevation due to the sparseness of the automatic rain station network that records in a sub-hourly time scale in the study area. If the station with the minimum difference in elevation was at a distance beyond twice SPP spatial resolution (20 km), we opted for the nearest station.

Once the appropriate rain station was identified and the precise or approximate time of landslide occurrence was known, we determined the possible rainfall event that triggered the landslide. We identified the time of landslide occurrence as the ending time of rainfall events. We accumulated the rainfall from the starting time of rainfall to the ending time. When the time of landslide occurrence was unknown, we identified the ending time of landslide as the peak rainfall intensity during the day of the landslide occurrence. The interval between the starting and ending times is the duration of the rainfall event. Considering the varying rainfall in time, identifying the starting time of rainfall events might be complicated. Therefore, we considered a minimum period of 24 consecutive hours of no rain to separate two rainfall events. In the end, we have a pair of accumulated rainfall and duration for each landslide event to derive rainfall thresholds (Section 3.3). The same procedure was applied to the SPP rainfall database extracted from the grid corresponding to the location of the reference rain stations.

For the purpose of the threshold performance evaluation, the non-triggering rainfall events were taken into account. Using the similar definition above, we extracted the non-triggering rainfall events from the period between the oldest and the most current landslide event in our inventory.

3.3. Calculation of rainfall thresholds

For this study, we adopted the frequentist method (M. T. Brunetti et al., 2010; Peruccacci et al., 2012) to derive an empirical rainfall threshold. The method assumes a threshold curve of power-law form, relating the accumulated rainfall E (mm) to the rainfall duration D (hour):

$$E = (\alpha \pm \Delta\alpha) \times D^{(\gamma \pm \Delta\gamma)} \tag{1}$$

where α is a scaling constant (the intercept), and γ is the shape parameter that defines the slope of the threshold curve. Multiple thresholds corresponding to different exceedance probabilities were derived, ranging from 1% to 50%. The exceedance probability level of 50% corresponds to the best-fit line of all (D,E) scatter points, while lower levels represent threshold lines parallel to the best-fit line. When the rainfall in the study area exceeds the threshold, a landslide is likely to occur.

In order to be statistically robust, we randomly selected 70% of the landslide-triggering rainfall events and used the remaining to assess the threshold performance. This procedure was repeated 100 times, allowing us to obtain mean and standard deviation of α and γ in Equation 1 and to construct a contingency table. The contingency table lists four possible outcomes with the threshold as a binary classifier of the rainfall conditions ((D, E) points) that triggered or did not trigger landslides. A landslide-triggering (D, E) located above the threshold is a true positive (TP), and below the threshold is a false negative (FN). A non-triggering (D, E) above the threshold is a false positive and below the threshold is a true negative (TN).

Using the contingency table, we calculated three skill scores, i.e., True Positive Rate (TPR) and False Positive Rate (FPR), as well as true skill statistic (TSS):

$$TPR = \frac{TP}{TP+FN} \tag{2}$$

$$FPR = \frac{FP}{FP+TN} \tag{3}$$

$$TSS = TPR - FPR \tag{4}$$

TPR represents the proportion of the landslide-triggering (D, E) above the threshold (correctly predicted), and FPR is the proportion of non-triggering (D, E) above the threshold (incorrectly predicted). TSS measures the performance of the rainfall threshold to separate the triggering- and non-triggering rainfall events, where value of 1 indicates the best performance and value of 0 or less suggests a performance no better than a random chance. TSS is also known as Hanssen and Kuipers discriminant (Hanssen and Kuipers, 1965).

For each exceedance probability, we classified the rainfall events (E, D) into four categories of a contingency (TP, FP, FN, and TN) and calculated TPR and FPR skill scores. We then constructed a receiver operating characteristic (ROC) graph (Fawcett, 2006) based on TPR and FPR to evaluate the predicting capability of rainfall threshold for different exceedance probability levels. The area under the ROC curve (AUC) measures the goodness of each dataset. AUC values range from 0 (perfectly inaccurate) to 1 (perfectly accurate). In general, an AUC of 0.5 indicates no discrimination (i.e., landslide/no-landslide triggering rainfall events), $0.5 < AUC < 0.7$ is considered poor, $0.7 \leq AUC < 0.8$ is considered acceptable, $0.8 \leq AUC < 0.9$ is considered excellent, and $AUC \geq 0.9$ is considered outstanding (Hosmer et al., 2013).

4. Results

4.1. Performance of GSMaP-GNRT and CMORPH-CRT

The capacity of GSMaP-GNRT and CMORPH-CRT in detecting the hourly rainfall observed by automatic rain stations in the study area is summarised in performance diagrams (**Figure 2**). Given the perfect scores of statistical metrics shown in Table 2, a perfect detection capacity lies in the upper right of the performance diagram. In general, the detection capacity of both SPPs over each station site lies in approximately the same location, i.e., near the centre for low rainfall intensities (Figure 2a-d) and lower left for higher rainfall intensity (Figure 2e-f). The performance diagrams suggest that the capability of SPPs in detecting rainfall at an hourly time scale tends to be poorer as the threshold of rain detection increases. In general, the performance of GSMaP-GNRT is comparable to that of CMORPH-CRT, and both SPPs do not exhibit a trend with regard to the station elevation. However, a clear distinction can be seen, this being shown through thetwo groups highlighted in the performance diagrams for the detection of low rain intensity (Figure 2a-d). Specifically, if we inspect this figure further, the lower group exhibiting poorer performance represents the performances of the SPPs over the stations located in leeward of the mountain and hill ranges, i.e., ARG Pakisdadu and ARG Temanggung. Except for BIAS, the performance indicator values of this group are persistently lower than those of the upper group.

POD values imply that <63% of low rainfall intensity observed by automatic rain stations in the study area are correctly detected by both SPPs (Figure 2a-d). Less than 26% of the rain rates ≥5 mm/h observed in the study area were correctly detected by GSMaP-GNRT and CMORPH-CRT (Figure 2e). The fraction even has a lower value for rain rates ≥10 mm/h, below 16% (Figure 2f). Along with low POD values, low SR values are observed as well. Since SR equals to 1 – false alarm ratio, the low SR values imply that the SPP algorithms detected a significant number of rains that did not occur. Less than 43% of low rain intensity detected by either GSMaP-GNRT or CMORPH-CRT were observed at the surface in the study area, and the proportion is even less (<24%) for higher rainfall intensity. The combination of low POD and SR values resulted in low CSI values, indicating that the overall fraction of rainfall correctly detected by both SPPs is relatively small. BIAS values suggest that both GSMaP-GNRT and CMORPH-CRT tend to overestimate the low-intensity rainfall (Figure 2a-d) and underestimate the high-intensity rainfall in our study area (Figure 2f). The SPPs skill in detecting low-intensity rainfall slightly varies from station to station. Overall, both SPPs have very low skill in detecting high rain intensity at an hourly time scale.

Based on the performance in detecting rain over various detection thresholds described above and the spread of the indicators in the performance diagram, we consider using 0.2 mm/h as the basis for rain/no-rain threshold in the subsequent analysis. At this rain detection threshold, the spread of BIAS values is the narrowest among other detection thresholds for low-intensity rainfall.
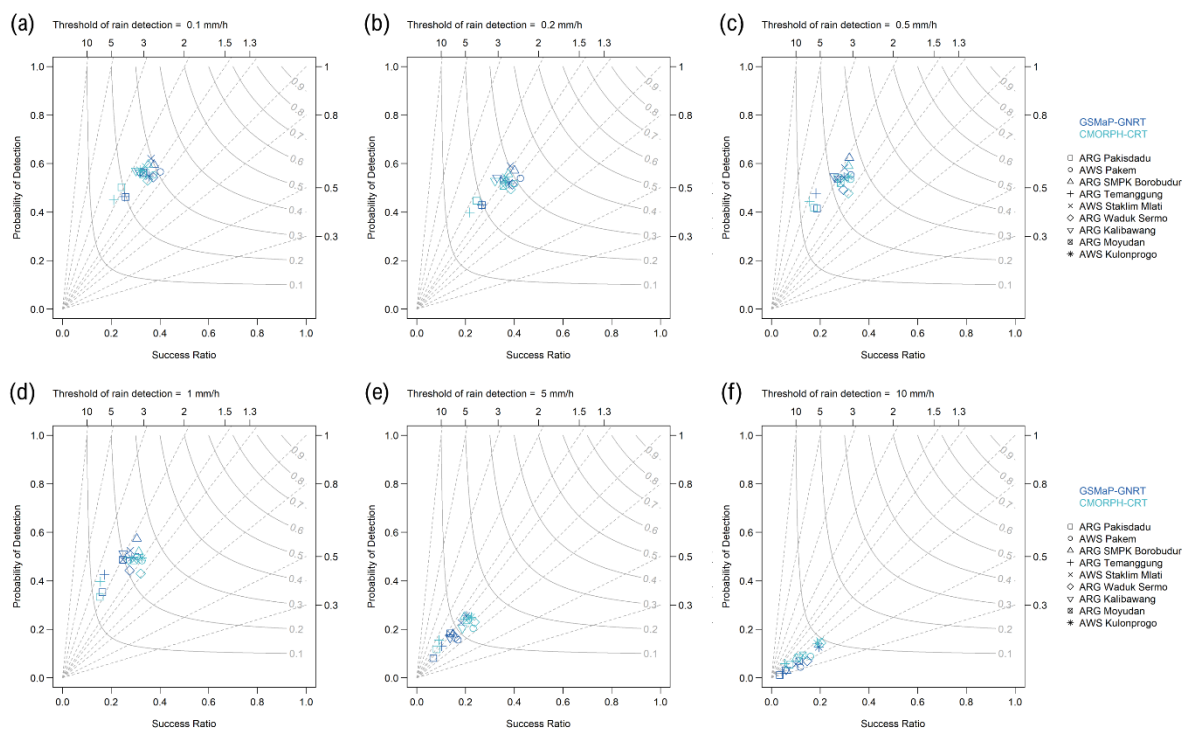
Figure 2. *Performance diagram summarising POD, SR, CSI, and BIAS of SPPs. Light grey contours represent CSI, whereas the dashed lines denote bias scores.*

Figure 3 shows a significant scatter between GSMaP-GNRT hourly rain estimates and the corresponding surface measurements at automatic rain stations in Progo Catchment. Few data points spread along the diagonal line, and false detection (missed rain) by the GSMaP-GNRT along the vertical (horizontal) axis are clearly observed. As shown in Figure 2, GSMaP-GNRT tends to overestimate the low intensity and underestimate high-intensity rainfall. However, most of the rain estimates and rain observed in the stations are low intensity. Therefore, GSMaP-GNRT exhibit very low CC at an hourly time scale (Table 3). This result suggests that GSMaP-GNRT could not reproduce hourly rainfall variation. Moreover, GSMaP-GNRT appears to provide rain estimates with a maximum value of ~30 mm/h.

Significant scatter also can be found between CMORPH-CRT rain estimates and the corresponding observed rain data from rain stations (**Figure 4**). The number of data points spread along the diagonal line is few, while false detection and missed rain are visible. Like GSMaP-GNRT, CMORPHT-CRT could not capture hourly rainfall observed in Progo Catchment.
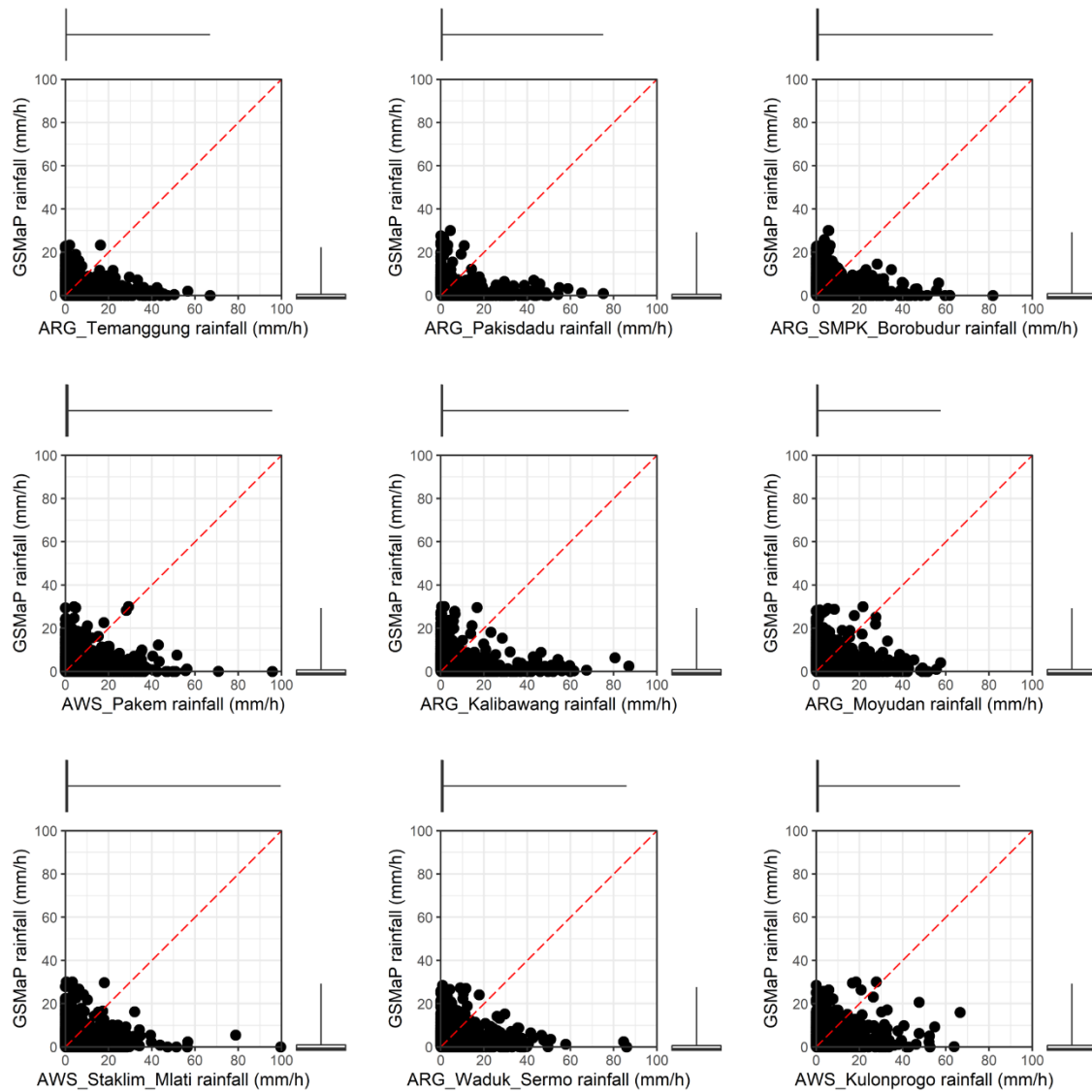
Figure 3. Scatter plots of GSMaP-GNRT and hourly rain rates observed at automatic rain stations in the study area. Each black dot represents a pair of observation with at least one of the data pair has value of ≥0.2 mm/h. Box and whisker plot at horizontal (vertical) axis shows the spread of observed rain at the station (GSMaP-GNRT rain estimates) at hourly time scale. The whiskers extend to the minimum and maximum values.
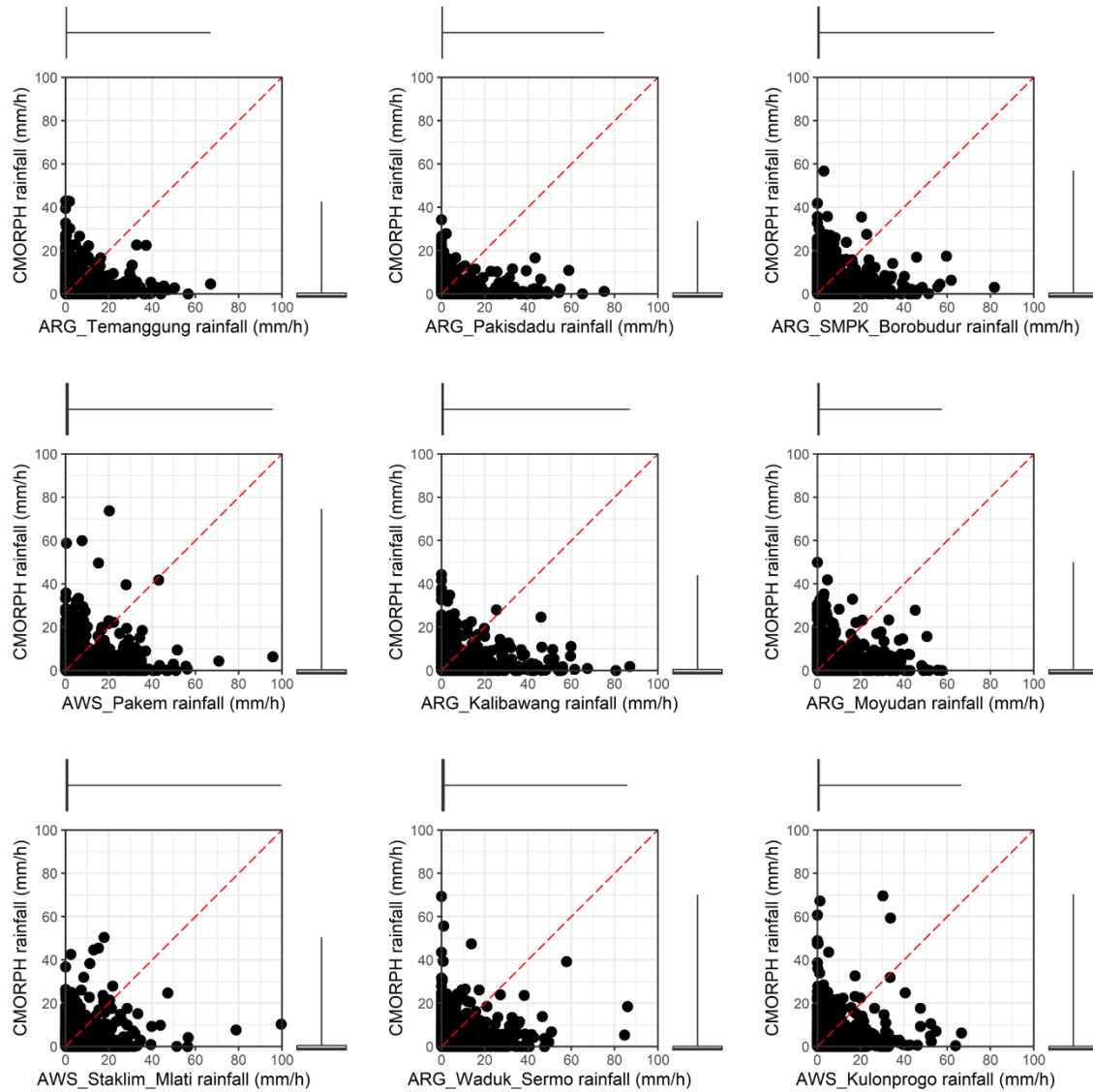
Figure 4. *Similar to Figure 3, but the scatter plots compare CMORPH-CRT and hourly rain rates observed at automatic rain stations in the study area.*

In general, the performance of GSMaP-GNRT in detecting rain ≥0.2 mm/h is comparable to that of CMORPH-CRT in terms of MAE, RB, and CC (*Table 3*). MAE and CC values are relatively unvarying from station to station in the Progo Catchment. GSMaP-GNRT has MAE values ranging from 2.32 mm (in Temanggung) to 3.03 mm (in Pakem), while MAE of CMORPH-CRT ranges from 2.37 mm (in Temanggung) to 2.94 (in Pakem). Regarding the RB indicator, RB values vary from station to station but do not show a trend regarding elevation. The values support the results shown in Figure 2b, where GSMaP-GNRT and CMORPH-CRT slightly overestimate the rain observed at almost all stations, except at AWS Pakem and ARG Waduk Sermo. The largest RB is observed at ARG Temanggung. The large bias is likely related to the fact that the station is located between two mountains on the leeward side. Regarding correlation, CC values show a very weak relationship between rain estimates obtained from each SPP and observed rain in all stations in Progo Catchment at an hourly time scale.

Table 3. Values of statistical metrics for hourly GSMaP-GNRT and CMORPH-CRT rain estimates with a rain detection threshold of 0.2 mm/h over Progo Catchment. TMG: ARG Temanggung, PKD: ARG Pakisdadu, SBR: ARG SMPK Borobudur, PKM: AWS Pakem, KLB: ARG Kalibawang, MYD: ARG Moyudan, SML: AWS Staklim Mlati, WDS: ARG Waduk Sermo, KLP: AWS Kulonprogo.

	TMG	PKD	SBR	PKM	KLB	MYD	SML	WDS	KLP
MAE									
GSMaP-GNRT	2.32	2.72	2.66	3.03	3.01	2.90	2.70	2.79	2.61
CMORPH-CRT	2.37	2.65	2.55	2.94	2.87	2.72	2.54	2.66	2.43
RB									
GSMaP-GNRT	0.40	0.12	0.16	-0.12	0.16	0.23	0.26	0.03	0.19
CMORPH-CRT	0.70	0.26	0.18	-0.09	0.11	0.12	0.21	-0.01	0.15
CC									
GSMaP-GNRT	0.03	-0.02	0.07	0.07	0.03	0.08	0.09	0.08	0.19
CMORPH-CRT	0.06	0	0.14	0.15	0.09	0.14	0.20	0.17	0.21

4.2. Empirical rainfall thresholds

The duration of rainfall events (D) measured by automatic rain stations that triggered landslides in Kulonprogo Catchment ranged from 1 hour to 289 hours (~12 days) with an average of ~87 hours. GSMaP-GNRT provided the duration of rainfall events triggering landslides ranging from 1 hour to 903 hours (~38 days) with an average of 130.5 hours. CMORPH-CRT produced a duration of rainfall events triggering landslides ranging from 1 hour to 387 hours (~16 days) with an average of ~90 hours. Note that the temporal resolution of the rainfall datasets to calculate the thresholds might partially contribute to the minimum duration of 1 hour.

As for the accumulated rainfall (E) triggering landslides, measurements by automatic rain stations shows the values ranged from 0.2 mm to 314.6 mm with an average of 102.2 mm. GSMaP-GNRT showed accumulated rainfall between 0.2 mm and 755.4 mm with an average of 121.9 mm. CMORPH-CRT produced accumulated rainfall as low as 0.2 mm and as high as 390.3 mm, with an average of 92.3 mm.

From the reconstructed rainfall events (D, E) for each dataset that triggered landslides in our landslide inventory, we calculated rainfall thresholds at several levels of exceedance probability. Table 4 presents equations of threshold curves defined from each dataset at several levels of exceedance probability, ranging from 1% to 50%. Close inspection of the equations shows that the station data generally produce the lowest thresholds at exceedance probability levels of 1%-20%. At exceedance probability levels of 20%-35%, station data exhibits only slightly lower thresholds than those derived from GSMaP-GNRT. However, station data produce slightly higher thresholds than GSMaP-GSMaP for D >17 hours, >1.3 hours, and >5.5 hours at exceedance probability levels of 40%, 45%, and 50%, respectively. Compared to CMORPH-CRT, the station data exhibit higher thresholds for shorter rainfall duration but higher for longer duration. The rainfall duration cut-off of this transition rises as the exceedance probability level increases. For instance, at an exceedance probability level of 5%, the station data produce a lower threshold for D <15 hours, while at an exceedance probability level of 20%, the data exhibit a lower threshold for D <5 days. Comparing the thresholds derived from GSMaP-GNRT and CMORPH-CRT, at exceedance probability levels of 1%-35%, GSMaP-GNRT consistently produces higher thresholds higher than CMORPH does, except for rainfall duration longer than ~11 days. At exceedance probability levels of 40%, 45%, and 50%,

CMORPH-CRT exhibits higher thresholds for rainfall duration longer than 7 days, 3 days, and ~6 days, respectively.

Table 4. Equations describing rainfall ED thresholds at different exceedance probability levels (labelled as T_x) derived for Progo Catchment. E is accumulated rainfall (in mm) and D is rainfall duration (in hour).

Dataset	Label	Equation
Automatic rain stations	T_1	$E = (-0.30 \pm 0.19) \times D^{(0.82 \pm 0.09)}$
	T_5	$E = (-0.10 \pm 0.19) \times D^{(0.82 \pm 0.09)}$
	T_{10}	$E = (0.01 \pm 0.19) \times D^{(0.82 \pm 0.09)}$
	T_{15}	$E = (0.09 \pm 0.19) \times D^{(0.82 \pm 0.09)}$
	T_{20}	$E = (0.15 \pm 0.18) \times D^{(0.82 \pm 0.09)}$
	T_{25}	$E = (0.20 \pm 0.18) \times D^{(0.82 \pm 0.09)}$
	T_{30}	$E = (0.25 \pm 0.19) \times D^{(0.82 \pm 0.09)}$
	T_{35}	$E = (0.30 \pm 0.19) \times D^{(0.82 \pm 0.09)}$
	T_{40}	$E = (0.34 \pm 0.18) \times D^{(0.82 \pm 0.09)}$
	T_{45}	$E = (0.35 \pm 0.17) \times D^{(0.82 \pm 0.09)}$
	T_{50}	$E = (0.37 \pm 0.17) \times D^{(0.82 \pm 0.09)}$
GSMaP-GNRT	T_1	$E = (-0.07 \pm 0.10) \times D^{(0.79 \pm 0.03)}$
	T_5	$E = (0.08 \pm 0.09) \times D^{(0.79 \pm 0.03)}$
	T_{10}	$E = (0.17 \pm 0.09) \times D^{(0.79 \pm 0.03)}$
	T_{15}	$E = (0.22 \pm 0.08) \times D^{(0.79 \pm 0.03)}$
	T_{20}	$E = (0.27 \pm 0.08) \times D^{(0.79 \pm 0.03)}$
	T_{25}	$E = (0.31 \pm 0.08) \times D^{(0.79 \pm 0.03)}$
	T_{30}	$E = (0.34 \pm 0.08) \times D^{(0.79 \pm 0.03)}$
	T_{35}	$E = (0.37 \pm 0.08) \times D^{(0.79 \pm 0.03)}$
	T_{40}	$E = (0.38 \pm 0.06) \times D^{(0.79 \pm 0.03)}$
	T_{45}	$E = (0.35 \pm 0.06) \times D^{(0.79 \pm 0.03)}$
	T_{50}	$E = (0.39 \pm 0.07) \times D^{(0.79 \pm 0.03)}$
CMORPH-CRT	T_1	$E = (-0.34 \pm 0.11) \times D^{(0.90 \pm 0.05)}$
	T_5	$E = (-0.19 \pm 0.10) \times D^{(0.90 \pm 0.05)}$
	T_{10}	$E = (-0.11 \pm 0.10) \times D^{(0.90 \pm 0.05)}$
	T_{15}	$E = (-0.05 \pm 0.10) \times D^{(0.90 \pm 0.05)}$
	T_{20}	$E = (-0.01 \pm 0.10) \times D^{(0.90 \pm 0.05)}$
	T_{25}	$E = (0.03 \pm 0.10) \times D^{(0.90 \pm 0.05)}$
	T_{30}	$E = (0.06 \pm 0.10) \times D^{(0.90 \pm 0.05)}$
	T_{35}	$E = (0.10 \pm 0.10) \times D^{(0.90 \pm 0.05)}$
	T_{40}	$E = (0.13 \pm 0.10) \times D^{(0.90 \pm 0.05)}$
	T_{45}	$E = (0.14 \pm 0.09) \times D^{(0.90 \pm 0.05)}$
	T_{50}	$E = (0.15 \pm 0.09) \times D^{(0.90 \pm 0.05)}$

Using the remaining 30% of the landslide-triggering rainfall events and the landslide non-triggering rainfall events, we assessed the performance of the thresholds. Figure 5 represents one out of 100 samples of derived rainfall thresholds at the exceedance probability level of 5% for three different datasets. The total number of rainfall events in each category of a contingency table for performance evaluation is also provided in Figure 5. Note that the number of landslide-triggering rainfall events captured by the three datasets might be different because rainfall data are sometimes unavailable. Figure 6 shows the constructed ROC describing the performance of the threshold at different levels of exceedance probability. It can be seen from Figure 5 that the

automatic rainfall station dataset provides slightly better performance compared to GSMaP-GNRT, particularly at an exceedance probability level below 15%. CMORPH-CRT performs the worst for all exceedance probabilities.

Further, a summary statistic of ROC in terms of AUC was calculated to be more objective. The results show that the AUC for automatic rainfall station, GSMaP-GNRT, and CMORPH-CRT are 0.72, 0.73, and 0.64, respectively. The AUC values also suggest that automatic rainfall station data and GSMaP-GNRT have acceptable capacity in discriminating the occurrence/non-occurrence of rainfall events resulting in landslides, while CMORPH-CRT has poor capacity.

Since the aim of defining rainfall thresholds is for an early warning system, it is essential to choose at which exceedance probability level the threshold provides the minimum number of false alarms (FP) and missed occurrences (FN). In other words, we find the threshold that maximises TPR and minimise FPR, and consequently maximises TSS, which is commonly applied (e.g., Leonarduzzi et al., 2017; M. T. Brunetti et al., 2018b). **Error! Reference source not found.** presents TSS scores at different exceedance probability levels of rainfall thresholds for the three datasets. The figure shows that the maximum TSS for automatic rain station data is achieved when the threshold is defined at an exceedance probability level of 10%. For GSMaP-GNRT (CMORPH-CRT) data, the highest TSS is obtained by defining the threshold at an exceedance probability level of 20% (15%) which also maximises TPR value.
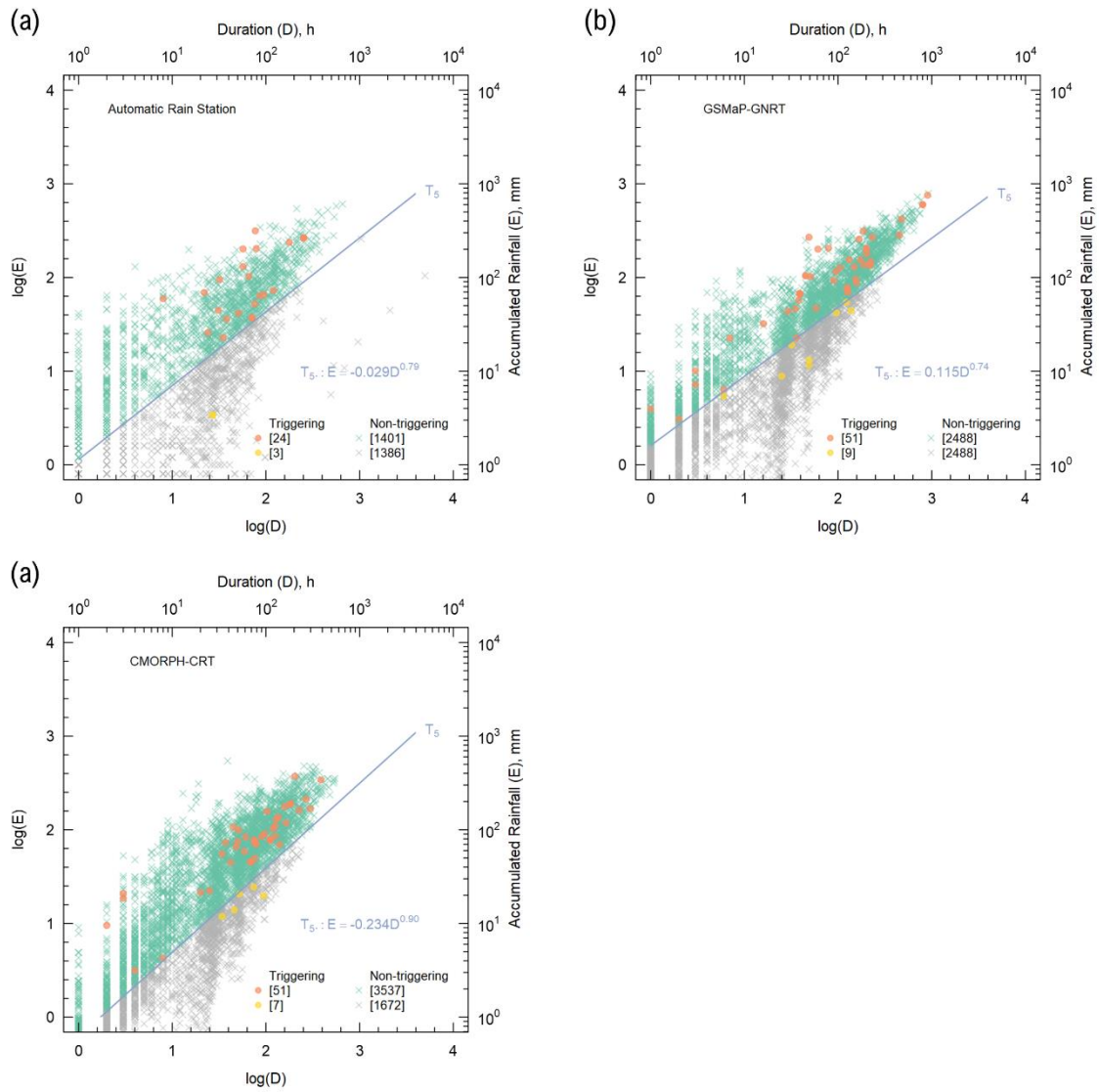
Figure 5. *A sample of rainfall thresholds at an exceedance probability of 5% derived from automatic rain stations (a), GSMaP-GNRT (b), and CMORPH-CRT (c) datasets using the frequentist method. The number inside the square bracket denotes the number of rainfall events (E-D pairs) corresponding to the categories in a contingency table.*
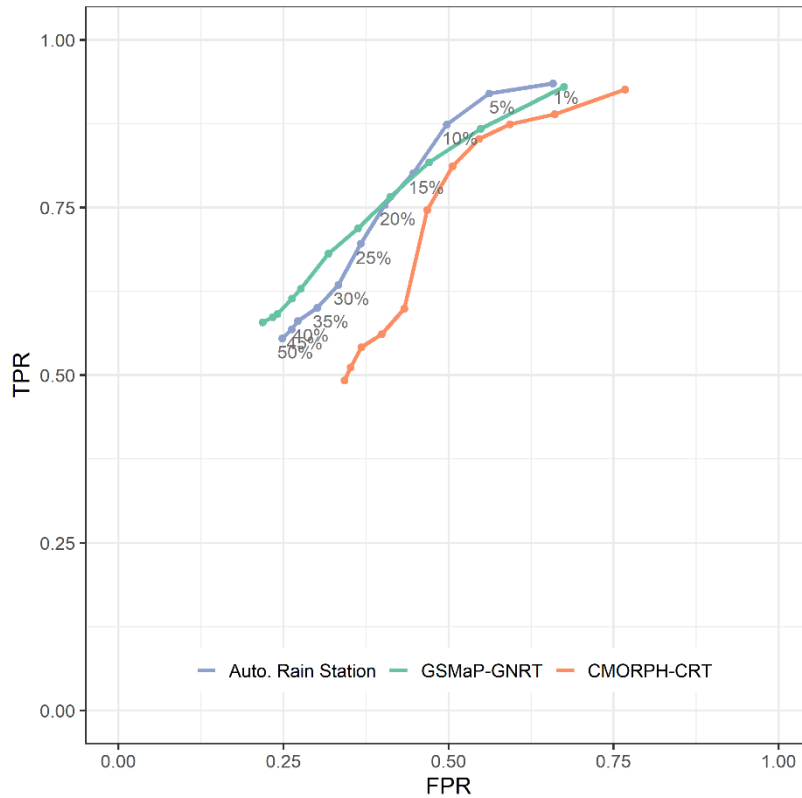
Figure 5. ROC curves built based on TPR and FPR skill scores for three datasets: automatic rain station (blue), GSMaP-GNRT (green), and CMORPH-CRT (orange). Each dot corresponds to the mean value of TPR and FPR skill scores of the repeated samplings. The labels beside the points represent the exceedance probability levels of rainfall thresholds.
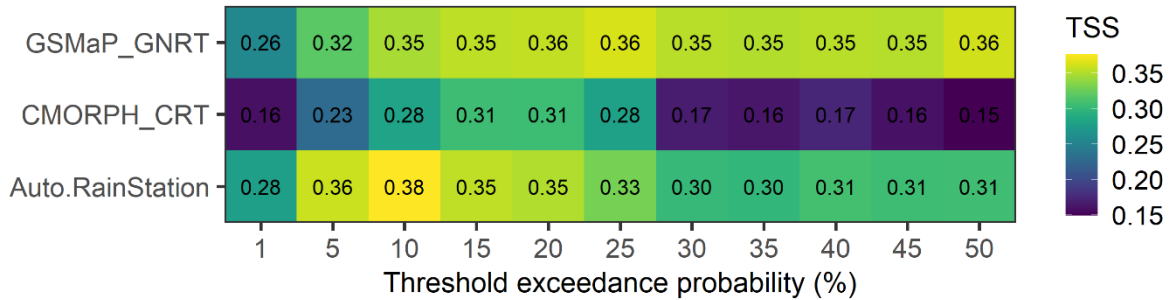

Figure 6. Values of True Skill Statistics (TSS) obtained at different exceedance probability levels of rainfall thresholds for the three datasets.

5. Discussion

This study was designed to estimate the empirical rainfall threshold for Progo Catchment based on rain gauge data and two SPPs, i.e., GSMaP-GNRT and CMORPH-CRT. Using the rain gauge data as ground truth for evaluating SPPs, this study found that the performance of GSMaP-GNRT and CMORP-CRT at an hourly time scale is less than excellent despite being corrected using gauge-based analysis data. Both SPPs tend to overestimate low-intensity rain and underestimate high-intensity

rain. Such tendency at the sub-daily scale was also reported for other regions with different climatic characteristics and varied topography, e.g., in Mexico (Bruster-Flores et al., 2019), Myanmar (Yuan et al., 2019), Ethiopia (Haile et al., 2013), and Tibetian Plateau (Li et al., 2021). The same tendency still persist at a daily time scale in different mountainous regions around the world (Derin et al., 2016). These results may be explained partially by the fact that both SPPs correct their rainfall estimates using the NOAA Climate Prediction Center (CPC) daily gauge analyses (Chen et al., 2008), whose accuracy depends on the rain gauge network density (Chen et al., 2008; Barros and Arulraj, 2020) and the representativeness of the gauges (Derin et al., 2016). Moreover, both SPPs perform poorly over mountainous areas despite the high spatial resolution and incorporation of an orographic rainfall detection scheme. This result is likely related to the technical limitations of satellite sensors in detecting orographic rainfall regarding ground-clutter effects, heterogeneity in the vertical and horizontal structure of cloud systems, satellite viewing angle, and overpass frequency (Barros and Arulraj, 2020).

The comparison results also show a weak correlation between SPP rainfall estimates and gauge observations. One explanation for this weak correlation is that the satellite algorithms failed to capture rainfall events with a duration shorter than or equal to satellite retrieval intervals (Haile et al., 2013). The point-area comparison also contributes to significant differences since high-intensity rainfall commonly occurs over an area much smaller than the SPP pixel size (Haile et al., 2013).

Another finding is that GSMaP-GNRT failed to capture rain rate >30 mm/h. This finding reflects that of Turk and Xian (2013), who also found that GSMaP products do not well capture the rainfall extremes at a sub-daily scale. Turk and Xian (2013) suggested that the failure could be attributed to the effect of Kalman filtering that averages the extreme values.

Aggregating rainfall into longer time scales results in better agreement between SPP and ground observations (e.g., Liu et al., 2020). Since the definition of rainfall events that trigger landslides includes accumulation of rainfall, hour-to-hour differences among the datasets are less significant than the total amount of rainfall accumulated during a rainfall event that potentially triggers landslides. Therefore, we also explore the determination of rainfall thresholds using the SPPs. Different from previous studies on rainfall thresholds for Indonesia that used daily rainfall for defining the thresholds for landslide EWS (Muntohar, 2008; Hidayat et al., 2019; Chikalamo et al., 2020; Muntohar et al., 2021; Yuniawan et al., 2022), our study utilises higher temporal resolution datasets and applies more robust statistical analysis. The usage of high temporal resolution is favoured to avoid more false alarms at shorter and missed events and at longer durations when the thresholds are implemented for operational landslide EWS (Gariano et al., 2020). Rainfall events determined from automatic rain stations, GSMaP-GNRT, and CMORPH-CRT that resulted in landslides have a duration of up to ~12 days, ~38 days, and ~16 days, respectively. These results indicate that landslides in Progo Catchment can also be triggered by less intense but prolonged rainfall. On the other hand, the existing EWS for landslides limited the antecedent days up to 3 days to define the threshold (Hidayat et al., 2019; Yuniawan et al., 2022). Therefore, it is possible that the amount of rainfall triggering landslides was underestimated by the existing LEWS.

The analysis of rainfall thresholds suggests that the rainfall measured at the stations performed slightly better than the estimated rainfall from GSMaP-GNRT, particularly at an exceedance probability level below 15% (Figure 6). Meanwhile, CMORPH-CRT performs the worst for all exceedance probabilities. These results accord with those of (M T Brunetti et al., 2018a), who compared various satellite-based rainfall products for landslide forecasting in Italy.

Based on TSS scores, the suitable exceedance probability for early warning purposes in Progo Catchment is 10% if it is based on the automatic rain station data. This value is slightly higher than the typical exceedance probability at which other studies applied the frequentist method, i.e., 5% (e.g., Vennari et al., 2014; Roccati et al., 2018; Leonarduzzi and Molnar, 2020) but within the threshold levels at 10%-25% suggested by Brunetti et al. (2018b). It is important to bear in mind that this direct comparison might be unfair because of the differences in data sources, resolution, climate, and the coverage area valid for the early warning.

6. Conclusion

This study aims to empirically determine the rainfall thresholds for landslides in Progo Catchment using various rainfall datasets via a frequentist approach. Our study is the first attempt to be more statistically rigorous than previous studies to determine the thresholds for a landslide-prone area in Indonesia. The results may assist the existing LEWS, which applies a fixed threshold limited to up to 3-days of rainfall amount. Conversely, we offer a dynamic window of rainfall events to determine rainfall thresholds that show a range of possible rainfall conditions in terms of accumulation and duration that trigger the landslides in the Progo Catchment.

Despite the high spatiotemporal resolution, both GSMaP-GNRT and CMORPH-CRT hourly products fail to capture high-intensity rainfall in Progo Catchment and overestimate light rainfall. This result seems to underline the challenge in remote sensing of rainfall in mountainous regions at appropriate spatial and temporal resolution for landslide studies, as Barros and Arulraj (2020) address. The poor capacity to detect high-intensity rainfall might limit the usage of SPP for hydrological modelling. Nevertheless, when accumulated to a duration of a rainfall event to derive the rainfall threshold, the overall performance of GSMaP-GNRT and automatic rain station data in Progo Catchment is comparable.

Being limited to the landslide events that occurred in Progo Catchment, the thresholds here might not be directly adopted in other areas due to the climatic regime differences that influence the local rainfall characteristics. The derived thresholds bear uncertainties due to the biased landslide inventory, as the events in remote locations might not have been reported. Moreover, the calculation of rainfall thresholds is not differentiated by whether the landslides occurred in urban or suburban areas.

For operational purposes, the thresholds defined here can adequately discriminate landslide-triggering and non-triggering rainfall conditions in terms of accumulation and duration. Maximising the TSS score offer the level at which exceedance probability should be applied for early warning that produces the minimum false alarms and missed events.

The major limitation of this study is that the satellite products have no prediction value, although the latency of the product is relatively short. Therefore, further study should be done using high-resolution numerical weather prediction (NWP) models that generate weather forecasts. Since both satellite products and NWP output have their uncertainties, it is unlikely to translate the thresholds here to thresholds for NWP output. Further study could also be conducted to assess the performance skills of NWPs in forecasting large/mesoscale weather systems producing the rainfall events that eventually could help advance the landslide early warning system.

References

Aldrian, E., and Susanto, R. D. (2003). Identification of three dominant rainfall regions within Indonesia and their relationship to sea surface temperature. *International Journal of Climatology*, *23*, 1435–1452. https://doi.org/10.1002/joc.950

Althuwaynee, O. F., Pradhan, B., and Ahmad, N. (2015). Estimation of rainfall threshold and its use in landslide hazard mapping of Kuala Lumpur metropolitan and surrounding areas. *Landslides*, *12*(5), 861–875. https://doi.org/10.1007/s10346-014-0512-y

Apip, Takara, K., Yamashiki, Y., Sassa, K., Ibrahim, A. B., and Fukuoka, H. (2010). A distributed hydrological – geotechnical model using satellite-derived rainfall estimates for shallow landslide prediction system at a catchment scale. *Landslides*, *7*, 237–258. https://doi.org/10.1007/s10346-010-0214-z

Barros, A. P., and Arulraj, M. (2020). Remote sensing of orographic precipitation. *Advances in Global Change Research*, *69*, 559–582. https://doi.org/10.1007/978-3-030-35798-6_6

BMKG. (2017). *Siklon Tropis "CEMPAKA" Lahir, Siaga Cuaca Ekstrem 3 Hari Ke Depan*. https://www.bmkg.go.id/berita/?p=siklon-tropis-cempaka-waspadai-hujan-lebat-disertai-angin-kencang-dan-gelombang-tinggi-di-wilayah-selatan-indonesia&tag=berita-utama&lang=ID

BNPB. (2021). *Data Informasi Bencana Indonesia*. http://dibi.bnpb.go.id/

Brunetti, M. T., Melillo, M., Peruccacci, S., Ciabatta, L., and Brocca, L. (2018b). How far are we from the use of satellite rainfall products in landslide forecasting? *Remote Sensing of Environment*, *210*, 65–75. https://doi.org/10.1016/J.RSE.2018.03.016

Brunetti, M. T., Peruccacci, S., Rossi, M., Luciani, S., Valigi, D., and Guzzetti, F. (2010). Rainfall thresholds for the possible occurrence of landslides in Italy. *Natural Hazards and Earth System Science*, *10*(3), 447–458. https://doi.org/10.5194/nhess-10-447-2010

Brunetti, M T, Melillo, M., Peruccacci, S., Ciabatta, L., and Brocca, L. (2018a). How far are we from the use of satellite rainfall products in landslide forecasting? *Remote Sensing of Environment*, *210*, 65–75. https://doi.org/10.1016/j.rse.2018.03.016

Brunetti, Maria Teresa, Melillo, M., Gariano, S. L., Ciabatta, L., Brocca, L., Amarnath, G., and Peruccacci, S. (2021). Satellite rainfall products outperform ground observations for landslide forecasting in India. *Hydrology and Earth System Sciences Discussions*, *February*, 1–27. https://doi.org/10.5194/hess-2021-42

Bruster-Flores, J. L., Ortiz-Gómez, R., Ferriño-Fierro, A. L., Guerra-Cobián, V. H., Burgos-Flores, D., and Lizárraga-Mendiola, L. G. (2019). Evaluation of precipitation estimates CMORPH-CRT on regions of Mexico with different climates. *Water (Switzerland)*, *11*(8), 1–15. https://doi.org/10.3390/w11081722

Cepeda, J., Smebye, H., Vangelsten, B., Nadim, F., and Muslim, D. (2010). *Landslide risk in Indonesia*.

Chen, M., Shi, W., Xie, P., Silva, V. B. S., Kousky, V. E., Higgins, R. W., and Janowiak, J. E. (2008). Assessing objective techniques for gauge-based analyses of global daily precipitation. *Journal of Geophysical Research*, *113*, D04110. https://doi.org/doi:10.1029/2007JD009132

Chikalamo, E. E., Mavrouli, O. C., Ettema, J., van Westen, C. J., Muntohar, A. S., and Mustofa, A. (2020). Satellite-derived rainfall thresholds for landslide early warning in Bogowonto Catchment, Central Java, Indonesia. *International Journal of Applied Earth Observation and Geoinformation*, *89*(May 2019), 102093. https://doi.org/10.1016/j.jag.2020.102093

Derin, Y., Anagnostou, E., Berne, A., Borga, M., Boudevillain, B., Buytaert, W., Chang, C. H., Delrieu, G., Hong, Y., Hsu, Y. C., Lavado-Casimiro, W., Manz, B., Moges, S., Nikolopoulos, E. I., Sahlu, D., Salerno, F., Rodríguez-Sánchez, J. P., Vergara, H. J., and Yilmaz, K. K. (2016). Multiregional satellite precipitation products evaluation over complex terrain. *Journal of Hydrometeorology*, *17*(6), 1817–1836. https://doi.org/10.1175/JHM-D-15-0197.1

Dunkerley, D. (2015). Intra-event intermittency of rainfall: an analysis of the metrics of rain and no-rain periods. *Hydrological Processes*, *29*, 3294–3305. https://doi.org/https://doi.org/10.1002/hyp.10454

Fawcett, T. (2006). An introduction to ROC analysis. *Pattern Recognition Letters*, *27*(8), 861–874. https://doi.org/10.1016/j.patrec.2005.10.010

Gubernur Daerah Istimewa Yogyakarta. (2017). *Keputusan Gubernur Daerah Istimewa Yogyakarta Nomor 261/KEP/2017 tentang Penetapan Status Tanggap Darurat Penanganan Bencana Banjir, Tanah Longsor, dan Angin Kencang*. https://www.birohukum.jogjaprov.go.id/produk_hukum_preview.php?id=13663

Guzzetti, F, Peruccacci, S., Rossi, M., and Stark, C. P. (2008). The rainfall intensity-duration control of shallow landslides and debris flows: An update. *Landslides*, *5*, 3–17. https://doi.org/10.1007/s10346-007-0112-1

Guzzetti, Fausto, Gariano, S. L., Peruccacci, S., Brunetti, M. T., Marchesini, I., Rossi, M., and Melillo, M. (2020). Geographical landslide early warning systems. *Earth-Science Reviews*, *200*(October 2019), 102973. https://doi.org/10.1016/j.earscirev.2019.102973

Hadmoko, D. S., Lavigne, F., and Samodra, G. (2017). Application of a semiquantitative and GIS-based statistical model to landslide susceptibility zonation in Kayangan Catchment, Java, Indonesia. *Natural Hazards*, *87*(1), 437–468. https://doi.org/10.1007/s11069-017-2772-z

Hadmoko, D. S., Lavigne, F., Sartohadi, J., Hadi, P., and Winaryo. (2010). Landslide hazard and risk assessment and their application in risk management and landuse planning in eastern flank of Menoreh Mountains, Yogyakarta Province, Indonesia. *Natural Hazards*, *54*(3), 623–642. https://doi.org/10.1007/s11069-009-9490-0

Haile, A. T., Habib, E., and Rientjes, T. (2013). Evaluation of the climate prediction center (CPC) morphing technique (CMORPH) rainfall product on hourly time scales over the source of the Blue Nile River. *Hydrological Processes*, *27*(12), 1829–1839. https://doi.org/10.1002/hyp.9330

Hanssen, A. W., and Kuipers, W. J. A. (1965). *On the Relationship Between the Frequency of Rain and Various Meteorological Parameters: With Reference to the Problem of Objective Forecasting* (Mededeling). http://bibliotheek.knmi.nl/knmipubmetnummer/knmipub102-81.pdf

Hapsari, R. I., Oishi, S., Syarifuddin, M., Asmara, R. A., and Legono, D. (2019). X-MP radar for developing a lahar rainfall threshold for the merapi volcano using a bayesian approach. *Journal of Disaster Research*, *14*(5), 811–828. https://doi.org/10.20965/jdr.2019.p0811

Hidayat, R., Sutanto, S. J., Hidayah, A., Ridwan, B., and Mulyana, A. (2019). Development of a Landslide Early Warning System in Indonesia. *Geosciences*, *9*(10), 451. https://doi.org/10.3390/geosciences9100451

Hong, M., Kim, J., and Jeong, S. (2018). Rainfall intensity-duration thresholds for landslide prediction

in South Korea by considering the effects of antecedent rainfall. *Landslides*, *15*(3), 523–534. https://doi.org/10.1007/s10346-017-0892-x

Hosmer, D. W., Lemeshow, S., and Sturdivant, R. X. (2013). *Applied Logistic Regression* (3rd Ed.). John Wiley and Sons.

Huffman, G. J., Adler, R. F., Bolvin, D. T., Gu, G., Nelkin, E. J., Bowman, K. P., Hong, Y., Stocker, E. F., and Wolff, D. B. (2007). The TRMM Multisatellite Precipitation Analysis (TMPA): Quasi-global, multiyear, combined-sensor precipitation estimates at fine scales. *Journal of Hydrometeorology*, *8*(1), 38–55. https://doi.org/10.1175/JHM560.1

Joyce, R. J., Janowiak, J. E., Arkin, P. A., and Xie, P. (2004). CMORPH: A method that produces global precipitation estimates from passive microwave and infrared data at high spatial and temporal resolution. *Journal of Hydrometeorology*, *5*(3), 487–503. https://doi.org/10.1175/1525-7541(2004)005<0487:CAMTPG>2.0.CO;2

Kahle, D., and Wickham, H. (2013). ggmap: Spatial visualization with ggplot2. *R Journal*, *5*(1), 144–161. https://doi.org/10.32614/rj-2013-014

Kidd, C., Becker, A., Huffman, G. J., Muller, C. L., Joe, P., Skofronick-Jackson, G., and Kirschbaum, D. B. (2017). So, how much of the Earth's surface is covered by rain gauges? *Bulletin of the American Meteorological Society*, *98*(1), 69–78. https://doi.org/10.1175/BAMS-D-14-00283.1

Kirschbaum, D., and Stanley, T. (2018). Satellite-Based Assessment of Rainfall-Triggered Landslide Hazard for Situational Awareness. *Earth's Future*, *6*(3), 505–523. https://doi.org/10.1002/2017EF000715

Kirschbaum, D., Stanley, T., and Zhou, Y. (2015). Spatial and temporal analysis of a global landslide catalog. *Geomorphology*, *249*, 4–15. https://doi.org/10.1016/j.geomorph.2015.03.016

Kubota, T., Aonashi, K., Ushio, T., Shige, S., Takayabu, Y. N., Kachi, M., Arai, Y., Tashima, T., Masaki, T., Kawamoto, N., Mega, T., Yamamoto, M. K., Hamada, A., Yamaji, M., Liu, G., and Oki, R. (2020). Global Satellite Mapping of Precipitation (GSMaP) Products in the GPM Era. In V. Levizzani, C. Kidd, D. B. Kirschbaum, C. D. Kummerow, K. Nakamura, & F. J. Turk (Eds.), *Satellite Precipitation Measurement. Advances in Global Change Research* (Vol. 67, pp. 355–373). Springer, Cham. https://doi.org/10.1007/978-3-030-24568-9_20

Kuleshov, Y., Kurino, T., Kubota, T., Tashima, T., Xie, P., Kuleshov, Y., Kurino, T., Kubota, T., Tashima, T., and Xie, P. (2019). WMO Space-Based Weather and Climate Extremes Monitoring Demonstration Project (SEMDP): First Outcomes of Regional Cooperation on Drought and Heavy Precipitation Monitoring for Australia and Southeast Asia. In J. Abbot & A. Hammond (Eds.), *Rainfall - Extremes, Distribution and Properties*. IntechOpen. https://doi.org/10.5772/INTECHOPEN.85824

Lagomarsino, D., Segoni, S., Fanti, R., and Catani, F. (2013). Updating and tuning a regional-scale landslide early warning system. *Landslides*, *10*(1), 91–97. https://doi.org/10.1007/s10346-012-0376-y

Leonarduzzi, E., and Molnar, P. (2020). Deriving rainfall thresholds for landsliding at the regional scale: Daily and hourly resolutions, normalisation, and antecedent rainfall. *Natural Hazards and Earth System Sciences*, *20*(11), 2905–2919. https://doi.org/10.5194/nhess-20-2905-2020

Leonarduzzi, E., Molnar, P., and McArdell, B. W. (2017). Predictive performance of rainfall thresholds for shallow landslides in Switzerland from gridded daily data. *Water Resources Research*, *53*(8), 6612–6625. https://doi.org/10.1002/2017WR021044

Li, Q., Wei, J., Yin, J., Qiao, Z., Peng, W., and Peng, H. (2021). Multiscale comparative evaluation of

the GPM and TRMM precipitation products against ground precipitation observations over chinese tibetan plateau. *IEEE Journal of Selected Topics in Applied Earth Observations and Remote Sensing*, *14*, 2295–2313. https://doi.org/10.1109/JSTARS.2020.3047897

Liu, C. Y., Aryastana, P., Liu, G. R., and Huang, W. R. (2020). Assessment of satellite precipitation product estimates over Bali Island. *Atmospheric Research*, *244*(April), 105032. https://doi.org/10.1016/j.atmosres.2020.105032

Muntohar, A. S. (2008). Toward Regional Rainfall Threshold for Landslide Occurrence in Yogyakarta and Central of Java. *Jurnal Teknik Sipil*, *III*(1), 1–8.

Muntohar, A. S., Mavrouli, O., Jetten, V. G., Van, C. J., and Hidayat, R. (2021). Development of Landslide Early Warning System Based on the Satellite-Derived Rainfall Threshold in Indonesia. In N. Casagli, V. Tofani, K. Sassa, P. T. Bobrowsky, & K. Takara (Eds.), *Understanding and Reducing Landslide Disaster Risk. WLF 2020. ICL Contribution to Landslide Disaster Risk Reduction* (pp. 227–235). Springer, Cham. https://doi.org/10.1007/978-3-030-60311-3

NCAR. (2015). *Package ' verification '* (1.42). https://cran.r-project.org/package=verification

Peruccacci, S., Brunetti, M. T., Gariano, S. L., Melillo, M., Rossi, M., and Guzzetti, F. (2017). Rainfall thresholds for possible landslide occurrence in Italy. *Geomorphology*, *290*, 39–57. https://doi.org/10.1016/j.geomorph.2017.03.031

Peruccacci, S., Brunetti, M. T., Luciani, S., Vennari, C., and Guzzetti, F. (2012). Lithological and seasonal control on rainfall thresholds for the possible initiation of landslides in central Italy. *Geomorphology*, *139–140*, 79–90. https://doi.org/10.1016/j.geomorph.2011.10.005

Priyambodoho, B. A., Kure, S., Yagi, R., and Januriyadi, N. F. (2021). Flood inundation simulations based on GSMaP satellite rainfall data in Jakarta, Indonesia. *Progress in Earth and Planetary Science*, *8*(1). https://doi.org/10.1186/s40645-021-00425-8

Rahmawati, N., and Lubczynski, M. W. (2018). Validation of satellite daily rainfall estimates in complex terrain of Bali Island, Indonesia. *Theoretical and Applied Climatology*, *134*(1–2), 513–532. https://doi.org/10.1007/s00704-017-2290-7

Rauniyar, S. P., Protat, A., and Kanamori, H. (2017). Uncertainties in TRMM-Era multisatellite-based tropical rainfall estimates over the Maritime Continent. *Earth and Space Science*. https://doi.org/10.1002/2017EA000279

Robbins, J. C. (2016). A probabilistic approach for assessing landslide-triggering event rainfall in Papua New Guinea, using TRMM satellite precipitation estimates. *Journal of Hydrology*, *541*, 296–309. https://doi.org/10.1016/j.jhydrol.2016.06.052

Roccati, A., Faccini, F., Luino, F., Turconi, L., and Guzzetti, F. (2018). Rainfall events with shallow landslides in the Entella catchment, Liguria, northern Italy. *Natural Hazards and Earth System Sciences*, *18*(9), 2367–2386. https://doi.org/10.5194/nhess-18-2367-2018

Roebber, P. J. (2009). Visualizing multiple measures of forecast quality. *Weather and Forecasting*, *24*(2), 601–608. https://doi.org/10.1175/2008WAF2222159.1

Rossi, M., Luciani, S., Valigi, D., Kirschbaum, D., Brunetti, M. T., Peruccacci, S., and Guzzetti, F. (2017). Statistical approaches for the definition of landslide rainfall thresholds and their uncertainty using rain gauge and satellite data. *Geomorphology*, *285*, 16–27. https://doi.org/10.1016/j.geomorph.2017.02.001

Sartohadi, J., Samodra, G., and Hadmoko, D. S. (2010). Landslide Susceptibility Assessment using Heuristic Statistically Method in Kayangan Catchment Kulon Progo Yogyakarta-Indonesia.

International Journal of Geoinformatics, *6*(3), 23–28.

Segoni, S., Rosi, A., Rossi, G., Catani, F., and Casagli, N. (2014). Analysing the relationship between rainfalls and landslides to define a mosaic of triggering thresholds for regional-scale warning systems. *Natural Hazards and Earth System Sciences*, *14*(9), 2637–2648. https://doi.org/10.5194/nhess-14-2637-2014

Tashima, T., Kubota, T., Mega, T., Ushio, T., and Oki, R. (2020). Precipitation Extremes Monitoring Using the Near-Real-Time GSMaP Product. *IEEE Journal of Selected Topics in Applied Earth Observations and Remote Sensing*, *13*, 5640–5651. https://doi.org/10.1109/JSTARS.2020.3014881

Turk, F. J., and Xian, P. (2013). An assessment of satellite-based high resolution precipitation datasets for atmospheric composition studies in the maritime continent. *Atmospheric Research*, *122*, 579–598. https://doi.org/10.1016/j.atmosres.2012.02.017

Ushio, T., Sasashige, K., Kubota, T., Shige, S., Okamoto, K., Aonashi, K., Inoue, T., Takahashi, N., Iguchi, T., Kachi, M., Oki, R., Morimoto, T., and Kawasaki, Z. I. (2009). A kalman filter approach to the global satellite mapping of precipitation (GSMaP) from combined passive microwave and infrared radiometric data. *Journal of the Meteorological Society of Japan*, *87A*, 137–151. https://doi.org/10.2151/jmsj.87A.137

Vennari, C., Gariano, S. L., Antronico, L., Brunetti, M. T., Iovine, G., Peruccacci, S., Terranova, O., and Guzzetti, F. (2014). Rainfall thresholds for shallow landslide occurrence in Calabria, southern Italy. *Natural Hazards and Earth System Sciences*, *14*(2), 317–330. https://doi.org/10.5194/nhess-14-317-2014

Wang, N., Cheng, W., Lombardo, L., Xiong, J., and Guo, L. (2021). Statistical spatiotemporal analysis of hydro-morphological processes in China during 1950–2015. *Stochastic Environmental Research and Risk Assessment 2021*, 1–21. https://doi.org/10.1007/S00477-021-02007-Y

Wild, A., Chua, Z. W., and Kuleshov, Y. (2021). Evaluation of satellite precipitation estimates over the south west pacific region. *Remote Sensing*, *13*(19), 1–16. https://doi.org/10.3390/rs13193929

Xie, P., Joyce, R., Wu, S., Yoo, S.-H., Yarosh, Y., Sun, F., and Lin, R. (2017). Reprocessed, Bias-Corrected CMORPH Global High-Resolution Precipitation Estimates from 1998. *Journal of Hydrometeorology*, *18*, 1617–1641. https://doi.org/10.1175/JHM-D-16-0168.1

Yin, H. Y., Lee, C. Y., and Jan, C. D. (2015). A web-based decision support system for debris flow disaster management in taiwan. In *Engineering Geology for Society and Territory - Volume 3: River Basins, Reservoir Sedimentation and Water Resources* (pp. 109–113). Springer International Publishing. https://doi.org/10.1007/978-3-319-09054-2_21/COVER

Yuan, F., Zhang, L., Soe, K. M. W., Ren, L., Zhao, C., Zhu, Y., Jiang, S., and Liu, Y. (2019). Applications of TRMM- and GPM-era multiple- satellite precipitation products for flood simulations at sub-daily scales in a sparsely gauged watershed in Myanmar. *Remote Sensing*, *11*(2). https://doi.org/10.3390/rs11020140

Yuniawan, R. A., Rifa'i, A., Faris, F., Subiyantoro, A., Satyaningsih, R., Hidayah, A. N., Hidayat, R., Mushthofa, A., Ridwan, B. W., Priangga, E., Muntohar, A. S., Jetten, V. G., Westen, C. J. van, Bout, B. V. den, and Sutanto, S. J. (2022). Revised Rainfall Threshold in the Indonesian Landslide Early Warning System. *Geosciences*, *12*(3), 129. https://doi.org/10.3390/geosciences12030129

Zhou, Z., Guo, B., Xing, W., Zhou, J., Xu, F., and Xu, Y. (2020). Comprehensive evaluation of latest GPM era IMERG and GSMaP precipitation products over mainland China. *Atmospheric Research*, *246*(March), 105132. https://doi.org/10.1016/j.atmosres.2020.105132